Entrainment of mammalian motile cilia in the brain with hydrodynamic forces

Nicola Pellicciotta[a], Evelyn Hamilton[a], Jurij Kotar[a], Marion Faucourt[b], Nathalie Delgehyr[b], Nathalie Spassky[b], and Pietro Cicuta[a,1]

[a]Cavendish Laboratory, University of Cambridge, CB3 0HE Cambridge, United Kingdom; and [b]Cilia Biology and Neurogenesis, Institut de biologie de l'Ecole Normale Supérieure, Ecole Normale Supérieure, CNRS, INSERM, Université Paris Sciences et Lettres, 75005 Paris, France

Edited by Howard A. Stone, Princeton University, Princeton, NJ, and approved February 14, 2020 (received for review June 12, 2019)

Motile cilia are widespread across the animal and plant kingdoms, displaying complex collective dynamics central to their physiology. Their coordination mechanism is not generally understood, with previous work mainly focusing on algae and protists. We study here the entrainment of cilia beat in multiciliated cells from brain ventricles. The response to controlled oscillatory external flows shows that flows at a similar frequency to the actively beating cilia can entrain cilia oscillations. We find that the hydrodynamic forces required for this entrainment strongly depend on the number of cilia per cell. Cells with few cilia (up to five) can be entrained at flows comparable to cilia-driven flows, in contrast with what was recently observed in *Chlamydomonas*. Experimental trends are quantitatively described by a model that accounts for hydrodynamic screening of packed cilia and the chemomechanical energy efficiency of the flagellar beat. Simulations of a minimal model of cilia interacting hydrodynamically show the same trends observed in cilia.

motile cilia | synchronization | multiciliated cell

Ciliated epithelia are fascinating examples of collective behavior in nature: Each single cilium beats in a nonreciprocal way along a defined direction and at the same frequency as the neighboring cilia, but with a different phase depending on its position. The result of this is "metachronal waves" that are able to drive a stable fluid flow along the surface carrying the carpet of cilia (1). This dynamics has long been known to have fundamental roles in organs of mammals and also in microorganisms (2). In the human airways, motile cilia generate flow for the clearance of mucus (3, 4). The multiciliated ependymal cells covering the ventricles in the brain ensure circulation of cerebrospinal fluid, thought to be necessary for brain homoeostasis, toxin washout, and migration of newborn neurons (5). Defects in ciliary motility cause many diseases such as bronchiectasis, hydrocephalus, and situs inversus (6). Although cilia coordination is required for the function of major organs, the mechanism behind it is still unclear. The role of hydrodynamic forces during developmental phases has been demonstrated: To generate a macroscopic flow efficiently, motile cilia must all beat in the same direction. As shown first in the ciliated larval skin of *Xenopus* (7), and then in mouse brain (8), multiciliated cells are responsive to external hydrodynamic forces, and align their beating direction when a physiologically relevant fluid flow is applied during development. It was suggested (8) that the cilia-driven flows could act to refine the cilia beating axis to a well-defined common direction, after an initial orientation bias provided by a cell prepatterning or by an external fluid flow. After achieving alignment, motile cilia beat at approximately the same frequency all over the tissue, with a constant phase difference with respect to the adjacent cilia (9). The current hypothesis is that cilia-driven flow could itself be the mechanical origin of this coordination (10). From the pioneering studies of Huygens in 1665, we know that oscillators with different intrinsic frequencies can reach synchronization if mechanically coupled (11). Cilia are microscopic filaments; the displaced fluid can act as a medium to transmit forces, so that the fluid velocity field couples all cilia (12). In the last decade, this hypothesis has been supported by simulations of pairs (13) and arrays of cilia (14–16) and experiments with cilia models (17, 18) and with ciliated microorganisms from the genus *Paramecium* (19, 20), *Chlamydomonas* (21), and *Volvox* (22, 23).

Alongside many reports supporting the importance of hydrodynamic coupling, recent experiments in *Chlamydomonas* (24–26) showed evidence that disrupting the elastic coupling through the cytoskeleton also affected flagellar synchronization. The authors of ref. 24 studied the phase locking between an external oscillatory flow and the *Chlamydomonas* flagella, measuring that the required hydrodynamic forces for phase locking are over an order of magnitude larger than the ones between flagella. They concluded that flagellar synchronization is due to elastic coupling. The importance of the flagellar inner coupling was also supported by theoretical studies (27, 28). This scenario suggests the possibility that cilia coordination might be achieved in nature in an organism-specific manner, thus leaving unclear what could be the underpinning mechanism in mammalian tissues. Motile cilia in mammalian cells are (inevitably) coupled, to some extent, through the cilia-driven flow, but are also structurally connected through the actin mesh that links elastically the bases of all cilia of the same cell (29–31). Even across confluent cells, the epithelium could be transmitting forces elastically. In principle, these basal connections could lead to synchronization (28), leaving the

Significance

We determine, in multiciliated mammalian cells, conditions for oscillatory flow to entrain brain motile cilia: Hydrodynamic forces of magnitude comparable to those generated by cilia themselves are sufficient to establish coordinated dynamics. We discuss this against recent reports on *Chlamydomonas* algae. Hydrodynamic screening between cilia plays an important role in entrainment: Cells with fewer cilia are much more susceptible to external flows. This changes how we should think about the physical mechanism underpinning collective cilia beating: It is not trivial to extrapolate from experiments on isolated cilia to the behavior of cilia assemblies, such as in multiciliated cells. Numerical simulations of a minimal mechanistic model recapitulate, qualitatively, the key results supporting the role of hydrodynamics.

Author contributions: N.P. and P.C. designed research; N.P. and E.H. performed research; N.P., E.H., J.K., M.F., N.D., and N.S. contributed new reagents/analytic tools; N.P. and E.H. analyzed data; and N.P., E.H., J.K., M.F., N.D., N.S., and P.C. wrote the paper.

The authors declare no competing interest.

This article is a PNAS Direct Submission.

Data deposition: A frequency scan dataset for a cell is available as a Zenodo repository, https://doi.org/10.5281/zenodo.3604352.

[1]To whom correspondence may be addressed. Email: pc245@cam.ac.uk.

This article contains supporting information online at https://www.pnas.org/lookup/suppl/doi:10.1073/pnas.1910065117/-/DCSupplemental.

First published March 26, 2020.

origin of cilia coordination in mammal organs still unresolved. Inspired by the experimental setup in ref. 24, we have tackled this problem by investigating the response of single multiciliated cells to hydrodynamic oscillatory flows. We find that phase locking of the motile cilia to the external flow (entrainment) is possible, and that it strongly depends on the number of cilia per cell (Fig. 1). Specifically, cells with few cilia (up to five) are very responsive to external flow, and they entrain with flow velocities comparable to those cilia of multiciliated epithelia can generate in vivo. By contrast, cells with higher number of cilia require much higher flow velocities to get entrained. We suggest that this effect is due to the hydrodynamic interactions between cilia in the same cell: Multiple cilia can hydrodynamically screen the forces applied by the external flow, making the entrainment more difficult as the number of cilia increase. We support this view by quantitatively matching the data with a minimal hydrodynamic model, accounting also for the chemomechanical energy efficiency of the cilium (32). In the absence of external flow, we measure an increase of the ciliary beating frequency (CBF) with the number of cilia per cell, also consistent with hydrodynamically coupled cilia with coordinated motility. The trends of our experimental data match with simulations of a minimal model of cilia interacting hydrodynamically, supporting the possibility that hydrodynamic coupling underpins all of the measured effects.

Results

Experimental Setup. Pure neural stem cells (NSC), isolated from neonatal mouse subventricular zone, are cultured in vitro to progressively differentiate into multiciliated ependymal cells (33). Cells were grown in a polydimethylsiloxane (PDMS) channel attached to a plastic membrane (Corning Insert), which we call a "Transwell chip" (Fig. 1*A* and *Methods*). This Transwell chip culture, in a six-well plate with glass bottom, was imaged in bright-field using a Nikon 60× 1.20 NA water immersion objective on an inverted microscope, kept at 37 °C and controlled pH using a custom chamber (see *Methods*). The inlet of the Transwell chip was connected to a custom-made fluid pump able to drive an oscillatory sinusoidal flow with defined frequency and velocity magnitude (Fig. 1*A*). We applied external oscillatory flows spanning in frequency f_{EX} from 10 Hz to 35 Hz, and a flow velocity v_{EX} (average during half cycle) from 200 μm/s to 2 mm/s. The lower value for v_{EX} was chosen to be close to the average net flow velocity created by ependymal cells in the brain (34). The applied range of frequency is chosen looking at the average CBF of the in vitro culture. As a calibration step, the flow created by the pump was measured from the trajectory of microparticle tracers at 7 μm from the cell surface (see *Methods*). In each experiment, a spatially isolated multiciliated cell was recorded for 5 s at 500 frames per second (fps) for each flow treatment, to extract CBF and phase. Recording started 5 s after the beginning of the flow treatment. We recorded only cells close to the center of the channel, beating in the same direction of the applied flow, and with a well-defined peak in the frequency distribution (more information is provided in *Methods*).

Entrainment of Multiciliated Cells with External Flow. We will refer to entrainment when we measure phase locking between the external flow and the cilia within a cell, while the term

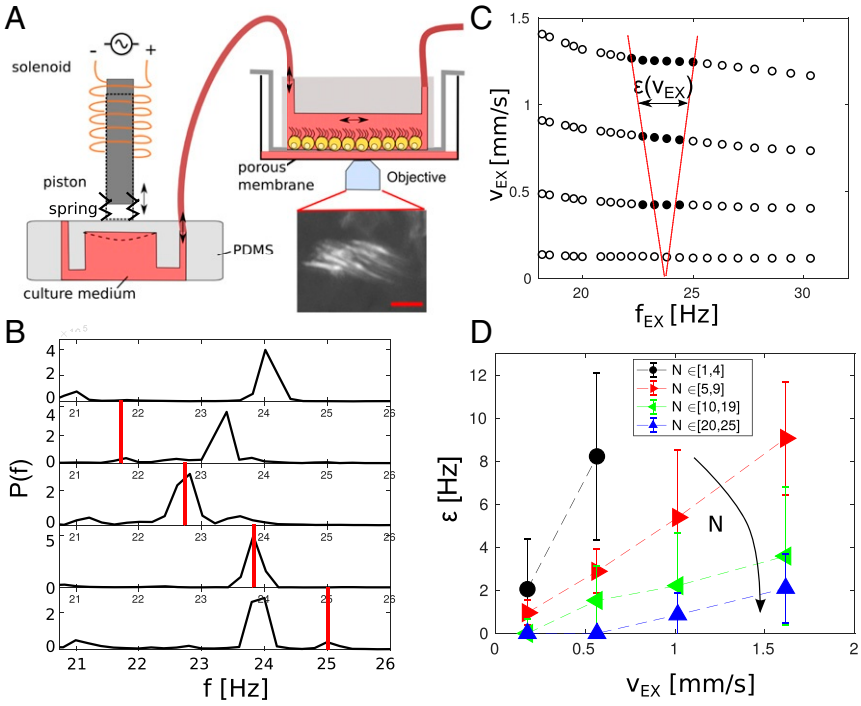

Fig. 1. The strength of hydrodynamic coupling can be measured experimentally by applying an external oscillatory flow to a ciliated epithelium, while imaging cilia motility. (*A*) Schematic of the experimental setup, showing motility in a ciliated cell through a map of SD in time. (Scale bar, 5 μm.) (*B*) The CBF is measured as the peak of the space-averaged periodogram of the pixel intensity over a cell, $P^S(f)$. The entrained state is defined as the peak of $P^S(f)$ being within 0.25 Hz of the external flow frequency f_{EX} (red line). Here, the applied external velocity is $v_{EX} = 0.6$ mm/s (average velocity during half-cycle). (*C*) Entrainment region, for the same multiciliated cell, in the frequency and flow velocity domain; each marker here is the result of a separate recording. Markers are dark (solid circles) when the average CBF of the cell matches the frequency of the external flow. The entrainment strength, $\epsilon(v_{EX})$, is the range of frequencies spanned horizontally by the black dots. The entrainment region is highlighted here as the area between the red dashed lines; lines are a guide to the eye. (*D*) The entrainment strength $\epsilon(v_{EX})$ increases proportionally to the applied external flow, but decreases with the number of cilia per cell, N_c. Each line is the average of this trend over a group of cells with similar number of cilia. Error bars represent the SD. Complete datasets are shown in *SI Appendix*, Fig. S9.

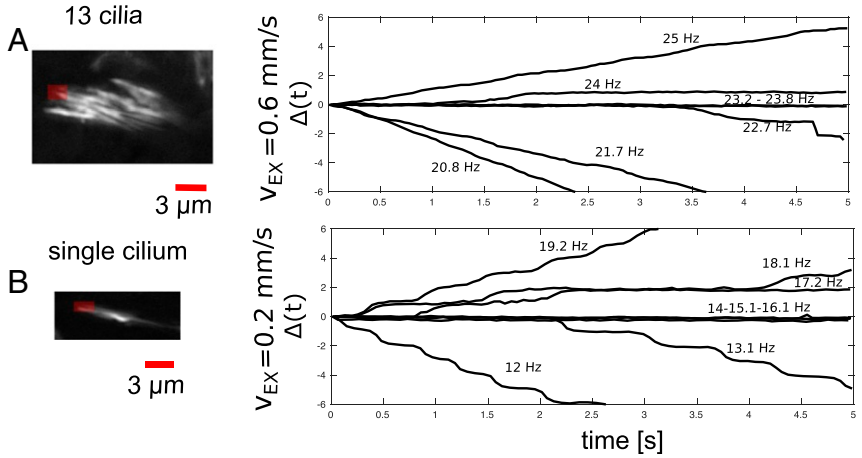

Fig. 2. The frequency and phase of each cilium, and the number of cilia per cell, are extracted from high frame rate video microscopy recordings. (*A*) Dynamics of the phase difference $\Delta(t)$ when an external flow of $v_{EX} = 0.6$ mm/s is applied on a cell with 13 cilia. (*B*) Data for a single cilium when an external flow of $v_{EX} = 0.2$ mm/s is applied. The phase difference is constant (phase locking) when the cilium is entrained by the external flow. The interrogation windows used are marked in red, over the SD maps. For the phase of the external flow, we used $\phi_{EX}(t) = 2\pi f_{EX} t + \phi_0$, where ϕ_0 is set such $\Delta(t = 0) = 0$.

synchronization will be used to indicate when many individual cilia coordinate their beating to a coherent collective beat pattern (35). The entrainment regimes for a multiciliated cell in the frequency and flow domain are shown in Fig. 1*C*, with each marker representing a separate recording. Solid markers identify an entrainment event, that is, when the measured CBF coincides with f_{EX}, the external flow frequency (more information is provided in *Methods*). The regimes seen here agree with the shape of an Arnold tongue, a general property of coupled phase oscillators, as was previously found for a pair of eukaryotic flagella of the *Chlamydomonas* algae under the effect of external flow (24), and in a hydrodynamic model oscillator system (36). From these data, one can define an entrainment strength $\epsilon(v_{EX})$ as the width of the frequency interval where entrainment is observed, and v_{EX} as the average magnitude of the applied oscillating flow. For values of v_{EX} and f_{EX} within the entrainment area, the phase difference between the cilium and the phase of the external oscillatory flow, $\Delta(t) = (\phi_{cilium}(t) - \phi_{EX}(t))/2\pi$, is constant over time ("locked") except for a few occasional phase slips (Fig. 2). During a phase slip, the cilia carry out one beat more (or less) with respect to the external driving, and thus $\Delta(t)$ increases (or decreases) of one unit. By contrast, when f_{EX} and v_{EX} are outside of the entrainment area, $\Delta(t)$ increases dramatically with time (Fig. 2). This behavior of $\Delta(t)$ resembles the general phase dynamics of a self-sustained oscillator under external forces and noise (35). Examples of the recordings that we used for the analysis are provided in *SI Appendix*, Figs. S2 and S3, with links to videos.

For each experiment, the CBF was measured averaging the time domain fast Fourier transform (FFT) spectra of pixel intensity over an area segmented over the multiciliated cell, similarly to standard cilia CBF analysis (37, 38). The cilia phase dynamics, $\Delta(t)$, can be found by tracking the passage of one cilium of the multiciliated cell in an interrogation window close to the position of the recovery strokes, as was done on algae (22); more information is provided in *Methods*.

Entrainment Depends on the Number of Cilia. Ciliated cells in culture (probably in contrast to most ciliated epithelia in vivo) are not always fully ciliated, and they exhibit a varying number of cilia per cell (*SI Appendix*, Fig. S13). We benefited from this situation, gathering results from 58 isolated multiciliated cells with different numbers of cilia. For each multiciliated cell, we measured the entrainment strength ϵ as a function of v_{EX}, the average magnitude speed of the oscillatory flow. We found that ϵ increases almost linearly with v_{EX}, consistent with a recent study on the eukaryotic flagella of *Chalmydomonas* algae (24) (Fig. 1*D*). Moreover, ϵ does not change significantly with the intrinsic (absence of external flow) CBF of the cells (*SI Appendix*, Fig. S6), but dramatically decreases with the number of cilia per cell (Fig. 1*D*). Markedly, cells with one to five cilia were entrained by the external flow over a frequency range with a width of around 2 Hz with flow velocity $v_{EX} \approx 200$ μm/s. In sharp contrast, cells with higher numbers of cilia were entrained over a detectable frequency interval only for strong flows $v_{EX} > 600$ μm/s. The linearity of ϵ with the external flow v_{EX} and its trend with the number of cilia are highlighted in Fig. 3*D* by showing the entrainment strength divided by the applied external velocity ($\epsilon(N)/v_{EX}$) as a function of N, the number of cilia per cell.

Hydrodynamic Screening Could Affect Entrainment of Motile Cilia. The observation that high forces are required to entrain larger clusters of cilia is not in contrast with the role of hydrodynamic coupling, because the external forces on each cilium could be hydrodynamically screened by the forces applied by the beating cilia nearby. This effect can be estimated: For an isolated cilium, the total drag force F_{EX} exerted by the external flow is proportional to the drag coefficient. If we assume each cilium as a rigid rod, its drag coefficient in the bulk is $\gamma = 4\pi\eta L/[\log(L/r) - 1/2]$ (39), with $r \ll L$ being, respectively, the radius and the length of the cilium, and η being the viscosity of the medium. In this case, the external drag force is $F_{EX} = \gamma v_{EX}$. For an ependymal cell with multiple cilia, the bases of the cilia are very densely and homogeneously concentrated in the centriolar patch located at the rear of the cell (29) (Fig. 3*A*), as we also see in our culture (Fig. 3*B*). Therefore, from the hydrodynamic point of view, a cluster of cilia all beating at the same frequency and phase can be modeled as a single impenetrable rod sticking out from a cell membrane. The effective rod has a length L and an effective radius $r_e(N) > r$ that contains all of the N cilia from the same cell (40). For notation purposes, we name this approximation the "Impenetrable Effective Rod" model (IER). We can then use the drag coefficient of this effective rod to estimate the hydrodynamic screening of the external flows due to the nearby cilia. $F^i_{EX}(N)$, the effective drag experienced by each cilium (i) in the cluster of N, is thus

$$F^i_{EX}(N) = \frac{\gamma_e(N) v_{EX}}{N}, \quad \gamma_e(N) = \frac{4\pi\eta L}{\log(L/r_e(N)) - 1/2}. \quad [1]$$

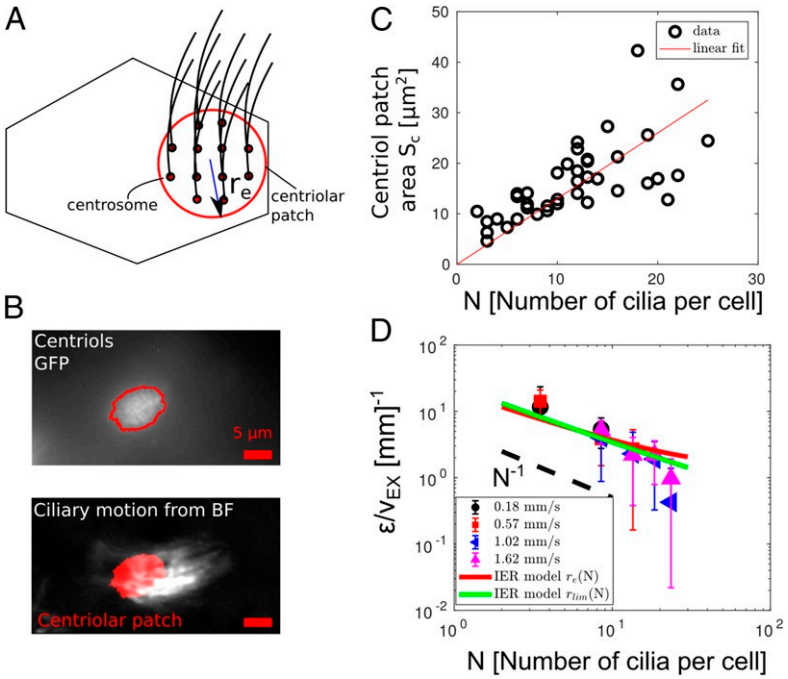

Fig. 3. How a cell is affected by an external flow depends on the number of motile cilia: The entrainment of cilia motility gets weaker, increasing the number of cilia, in agreement with a model where the external forces are hydrodynamically screened by the nearby cilia. (*A*) Cilia within an ependymal cell are very densely packed at the rear of the cell, and are anchored at the cell membrane in the centriolar patch. The cluster of beating cilia can be hydrodynamically approximated as a single impenetrable effective rod, with the same size as the centriolar patch. (*B*) Cen-GFP mice can be used to measure the size of the centriolar patch, in living cells before the flow experiments. (*Top*) Cilia centrioles are shown in white (GFP). Stimulated emission depletion microscopy would be necessary to resolve the single centriole (29). We use these images only to measure the total area of the centriolar patch. The area is obtained by using Otsu's threshold method (red borders). (*Bottom*) The measured centriolar patch is superposed to the cell motility map extracted from BF images. (*C*) The area of the centriolar patch S_c increases roughly linearly with the number of cilia (linear fit R-squared =0.4). We used these data to find an analytic expression for the r_e as a function of the number of cilia that can be plugged into the IER model. (*D*) The measured entrainment strength decreases with the cilia number and collapses onto a single set when divided by the applied the external velocity ($\epsilon(N)/v_{EX}$). Here we show the median binned data with standard deviations. The complete dataset is shown in *SI Appendix*, Fig. S10. The trend with the number of cilia is well matched with the proposed model, using a single fit parameter F_{dr}. We show the fit results using as effective radius 1) $r_e(N)$, equal to the centriolar patch size (R-squared =0.67), and 2) $r_{lim}(N)$, which is the limit case where cilia are touching (R-squared =0.69). The length of the effective rod is $L = 11$ μm, and medium viscosity is $\eta = 10^{-3}$ Pa·s for both fits.

We take the area of the centriolar patch $S_c(N)$ to quantify the effective radius of the rod as a function of the number of cilia within a cell: $r_e(N) = (S_c(N)/\pi)^{-1/2}$. We used transgenic mouse cells Cen2-GFP (41). This allows visualization of the base of the cilium (centrosome) in the living cells (29). We measured the area of the centriolar patch $S_c(N)$ for some of the cells treated with the oscillatory flow (Fig. 3*B*). This number increases linearly with the number of cilia, so that $r_e(N) \approx CN^{1/2}$, with $C = 0.6 \pm 0.1$ μm (Fig. 3*C*). This value is in agreement with another estimate of the effective radius derived from the dynamic area spanned by the moving cilia (*SI Appendix*, Fig. S11). In this scenario, the density of cilia in the effective rod is always constant, $\rho_c = N/\pi r_e^2 = 1/(C^2\pi) \approx 0.9$ cilia per μm^2. It is worth noting that, for cells with $N > 25$, we then estimate an effective radius of $r_e > 3$ μm $\approx L/4$. For such aspect ratios, we expect the slender body assumption in Eq. **1** to lose accuracy.

We can compare this situation with one where cilia are so densely packed that they are in contact: The spacing between neighboring cilia would be $2r$, where r is the radius of the single cilium. Then the section area of the effective rod could be approximated by $\pi r_{lim}^2(N) \approx N(2r)^2$. Also, in this case, the effective radius increases with the root of N, $r_{lim} \approx C_{lim}N^{1/2}$ with $C_{lim} = 2r/\sqrt{\pi} \approx 0.11$ μm, and cilia density is constant: $\rho_c^{lim} \approx 26$ cilia per μm^2. In both scenarios, we expect the term $O(1/N)$ in Eq. **1** to lead, and the drag on each cilium to decrease, as the number of cilia nearby increases, $F_{EX}^i(N+1) < F_{EX}^i(N)$. As the force applied by the external flow decreases, we expect to also have a drop in the entrainment.

The expression in Eq. **1** permits quantification of the force applied on each cilium by the external flow, as the number of cilia per cell increases. We can check whether this approximation is in agreement with the measured data. Here we use, as a minimal cilia model, a two-state oscillator in viscous liquid, driven by linear potential and entrained to an external periodic force (geometric rower model) (36); see also *SI Appendix*, section 1. The molecular motors acting on the cilium are coarse-grained, with a driving constant force F_{dr} applied to a sphere or a cylinder representing the cilium (18). The constant force F_{dr} switches in sign when a particular limit configuration is reached ("geometrical switch") so that the rower is pushed in the opposite direction; see also Fig. 5*A*. The limit configurations can be set at the edges of a path of length A, so that the rower undergoes longtime periodic motion with amplitude A and frequency $f = \mathrm{CBF}_0 = F_{dr}/(2A\gamma)$, where γ is the drag coefficient of the rower. On top of this force, we can add an external constant force F_{EX} to the rower, for example, given by an external flow. This force can be set to switch in sign according to the defined external frequency f_{EX}, and mimic the oscillatory external flow in our system. For this geometrical rower model, an analytic solution for the entrainment strength of the rower with the external oscillatory force has been found in ref. 36, highlighting a linear dependence of entrainment on the ratio of the driving and external forces. See

SI Appendix, section 1 for more details. The entrainment strength is thus

$$\epsilon(N) = \frac{2(\mathrm{CBF}_0)F^i_{EX}}{F_{dr}}. \quad [2]$$

Entrainment Strength on Multiciliated Regions Can Be Explained as an Effect of Hydrodynamic Screening. We now compare data with the consideration on screening from above. The CBF_0 is the BF of the cilium in the absence of external forces. In the cell cultures, the CBF of isolated cilia were measured to be $\mathrm{CBF}_0 \simeq 15$ Hz (Fig. 3*C*). The force applied by the external flow on a cilium is given by Eq. **1**, $F^i_{EX} = \gamma_e(N) v_{EX}/N$, with v_{EX} as the average magnitude speed of the oscillatory fluid flow. On the other hand, we assume the driving force F_{dr} as an intrinsic parameter of the cilium, therefore independent of N and v_{EX}. The driving force can be calibrated from the motion of the single cilium, in the absence of any external flow. The latter has to balance the hydrodynamic drag F^h_{dr} experienced by the cilium while moving with frequency CBF_0 and amplitude A. We again assume the cilium has the drag coefficient of a rigid cylinder and beats with amplitude $A \simeq L \approx 11$ μm. Then, the driving force is equal to the hydrodynamic drag $F^h_{dr} = \gamma 2A(\mathrm{CBF}_0) \simeq 11$ pN. The relation of the entrainment strength to the external forces may be dependent on the intricate molecular response of the individual motors within a cilium (42) and on the chemomechanical efficiency of the ciliary beat (32); in the biological system, the driving force has to balance the fluid viscous drag but also the intraciliary friction given by viscoelastic structural elements in the cilium, such as Nexin linkers (32, 43, 44). Inspired by the work of ref. 32, we consider internal friction forces to be proportional to the hydrodynamic drag experienced by the cilium while beating. The total driving force can then be written as $F_{dr} = F^h_{dr}/\eta_c$, where $\eta_c < 1$ is the chemomechanical efficiency of the ciliary beat. More details can be found in *SI Appendix*, section 1. Finally, for the cilium i, in a bundle of other N cilia arranged in a hydrodynamically impenetrable cylindrical rod of radius $r_e(N)$ and length L, we have

$$\frac{\epsilon(N)}{v_{EX}} = \frac{2\ \mathrm{CBF}_0}{(F^h_{dr}/\eta_c)} \frac{4\pi\eta L}{N[\log(L/r_e(N)) - 1/2]}. \quad [3]$$

We can fit this model to our data using the effective radius r_e found previously from experimental data, with the beating efficiency η_c as a single fit parameter. Results are provided in Fig. 3*D*. We find the driving force $F_{dr} = F^h_{dr}/\eta_c = 60 \pm 3$ pN, with R-squared=0.67. From this, we can estimate the chemomechanical ciliary beating efficiency $\eta_c = F^h_{dr}/F_{dr} = 0.18 \pm 0.01$, a value in remarkable agreement with the ones estimated by previous works, where $\eta_c \in [0.2, 0.4]$ (32, 44). It is worth noting that the experimental values are significantly lower in the cells with $N > 20$ (outliers of the error bars to this trend); this difference could be due to the fact that the slender body assumption in Eq. **1** is not very accurate in this regime, where $r_e \approx L/4$.

The same fit was performed using the effective radius r_{lim} in the situation of cilia touching (Fig. 3*D*). For this limit case, we find $F_{dr} = 30 \pm 3$ pN, with R-squared =0.69. With this number, we can estimate a chemomechanical ciliary beating efficiency of $\eta_c = 0.36$, which is still in agreement with the past literature (32, 44). The results are shown in Fig. 3*B*. While the distances between cilia basal bodies are set by the cytoskeleton in the cell, we cannot exclude that, when cilia are entrained to move at the same frequency, they might tend to be closer. For example, simulations have confirmed that hydrodynamic interactions due to the fluid flow generated by the flagella can lead to bundling of *Escherichia coli* flagella (45). Hydrodynamic attraction was also reported in simulations of swimming filaments (46). Moreover, in colloids driven by optical tweezers along circular paths, doublet clusters spontaneously arise by the hydrodynamic interactions between the particles (47). Despite its simplicity, the hydrodynamic model with two different estimates of the effective radius explains quantitatively the measured trend. Moreover, it leads to a value for the mammalian ciliary beating efficiency that is in agreement with other ciliated organisms.

CBF Increases with the Number of Cilia per Cell. Previous theoretical works (10, 14) predicted that arrays of beating cilia speed up their frequency, with respect to their intrinsic beating when hydrodynamically synchronized, reaching a maximum increase when cilia are beating in phase. Also, in our model, the fact that cilia from the same cell behave as a unique rigid rod would imply that the average CBF (in the absence of external flow) should increase with the number of cilia per cell. We again assume the molecular motors acting on the cilium to be coarse-grained into a constant driving force F_{dr} switching in sign at defined limit configurations (18). In the absence of interacting cilia, this driving force is equal to the sum of the hydrodynamic drag and the internal ciliary friction (32). The force balance equation can be written as $F_{dr} = 2A\gamma[\mathrm{CBF}_0] + 2A\gamma[(1-\eta_c)/\eta_c][\mathrm{CBF}_0]$, where $\gamma[(1-\eta_c)/\eta_c]$ is the intercilium friction coefficient and η_c is the chemomechanical ciliary beating efficiency defined in the previous paragraph, and γ is the cilium drag coefficient. In a multiciliated cell with N cilia, our IER assumption states that each cilium $i \leq N$ has drag coefficient γ_e/N, reduced by the hydrodynamic screening of nearby cilia (Eq. **1**). Now the driving force on this cilium F^i_{dr} can be written as $F^i_{dr} = 2A(\gamma_e(N)/N)[\mathrm{CBF}] + 2A[(1-\eta_c)/\eta_c]\gamma[\mathrm{CBF}]$. We assume the driving force is an intrinsic property of the cilium and independent of the cilia number, $F_{dr} = F^i_{dr}$. Thus we find

$$\mathrm{CBF}(N) = \frac{\mathrm{CBF}_0}{1 - \eta_c + \eta_c[\gamma_e(N)/(\gamma N)]}. \quad [4]$$

The above equation describes a saturating curve for $\mathrm{CBF}(N)$ as a function of the number of cilia within a cell. The ciliary beating efficiency sets the maximum value for the CBF at large N: $\mathrm{CBF}_{\max} = \mathrm{CBF}_0/(1-\eta_c)$. We compare this theoretical trend with the CBF gathered from 120 cells. In Fig. 4*A*, we show the theoretical curves using η_c and $\gamma_e(N)$ obtained from the previous experiments with external flows considering the two scenarios of cilia touching (green line r^{lim}_e) and cilia separated by the same distance of the basal bodies (red line r_e). For the former case, the value for $\mathrm{CBF}_{\max}$ seems to agree with the measured one, although the theoretical CBF increase at small N is sharper than the one we observed. Regarding the latter case, the theoretical CBF increase seems to be always lower than the average measured trend, although theoretical values are still within the error bars. From the fit of the data with Eq. **4** (two free parameters), we obtain $\eta^{CBF}_c = 0.4 \pm 0.2$, which is still in agreement with previous works (32, 44), and $C^{CBF} = 0.7 \pm 0.4$ μm, where the effective radius of the cilia bundle is $r^{CBF}_e = C^{CBF}\sqrt{N}$, again in agreement with our previous measurement of cilia distance within a cell. The differences between the values obtained from this fit and the values from the previous experiments could be due to the fact that cilia are not always beating coherently in the absence of external flows. We estimated the degree of cilia synchronization for each cell (in the absence of external flows) using the frequency spatial noise $\xi_s = \sigma_f/(\mathrm{CBF})$, where σ_f is the SD of the frequencies calculated on 4×4 pixel boxes over each cell, while the CBF is the median; see, for example, the frequency map in Fig. 4*B* and *SI Appendix*, Fig. S8. We found the spatial noise to be significantly different from zero for all of the cells examined, highlighting that cilia in the same cell do not beat as a unique entity, as assumed by our IER model, but with a

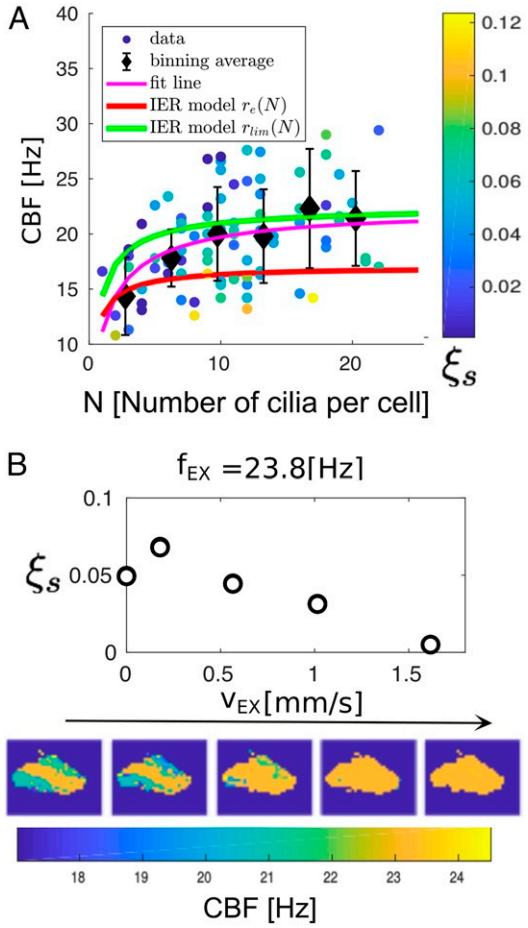

Fig. 4. In the absence of external flow, the CBF increases with the number of cilia. (*A*) Individual (and binned) CBF for 120 cells as a function of the number of cilia. Error bars are the SD of the binned data. The color of the unbinned data indicates the value of spatial noise ξ_s for each cell. A high value indicates that cilia within cells are beating at a different frequency and so are very far from the IER model assumptions. Interestingly, the average value of ξ_s for cells with cilia $N < 20$ is $\langle \xi_s \rangle_{N<20} = 0.04 \pm 0.02$, while it is almost double for the cells with a larger number of cilia, $\langle \xi_s \rangle_{N>20} = 0.07 \pm 0.02$. The red and the green line show the predicted trends of the CBF if cilia were behaving as single impenetrable rods (IER model) using the values found in the previous experiments with external oscillatory flows. The red line assumes cilia average distance dictated by the basal bodies distance, and the green line is the limit case of cilia touching. The purple line is a fit with two free parameters (η_c and C^{CBF}). (*B, Top*) The spatial noise of a ciliated cell decreases when cilia are entrained to an external flow. This is shown with one cell as an example: Each marker of spatial noise was calculated using a frequency map, illustrated in *Bottom*, with the color corresponding to the measured frequency in each 4 × 4 pixel box.

finite frequency detuning. In *SI Appendix*, Fig. S8, we show the CBF plotted against the spatial noise. By contrast, when cilia are entrained with the external flow, the spatial noise significantly decreases (Fig. 4*B*), explaining qualitatively why the IER assumption of Eq. **1** can be only valid during entrainment. This effect is expected to reduce the hydrodynamic screening between cilia with respect to the one expected from the IER model, and, in turn, to lead to a less sharp growth of the CBF with the number of cilia. Moreover, it is worth noting that cells with a larger number of cilia have, on average, a higher spatial noise ξ_s (Fig. 4*A*). The large difference between the CBF within the same cell may be also the reason why the measured entrainment strength is lower than the expected one from our model for cells with a large number of cilia (Fig. 3*B*).

From our measurements, CBF seems to reach a plateau value for cells with $N > 20$ that is roughly 50% higher compared to the ones with only a few cilia. A similar CBF increase with cilia number was measured after cells were treated with actin drug Cytochalasin-D, which progressively depolymerizes the actin network connecting the centrioles in the cells and at the cell border (29, 31) (*SI Appendix*, Fig. S7), suggesting that the observed CBF increase with cilia number is not due to cytoskeleton coupling.

Estimation of the Flow Generated by Cilia within a Cell. Hydrodynamic screening effects and interciliary dissipation seem to quantitatively describe the observed trend of CBF and entrainment strength with the number of cilia. We now assume that the observed trend of the CBF with the number of cilia is only due to hydrodynamic forces between cilia. This assumption is also motivated by the fact that CBF increase was not affected after depolymerization of the cell actin network, supporting the hypothesis that the measured effect is not driven by the elastic forces transmitted through the cytoskeleton. Moreover, we argue that steric interactions between cilia cannot be responsible for an increase of the average CBF (*SI Appendix*, section 3). In this limit scenario, we can use the same minimal model to roughly estimate the magnitude of the flow on the cilium i created by nearby cilia $j \neq i \in N$ in the absence of i. It is now convenient to write an explicit expression for the average hydrodynamic forces applied by nearby cilia during half-cycle of the beating. The sum of these forces we now define as F^i_{nc}, acting on the cilium i in a cell of N cilia. We can write a force balance equation on the cilium i averaged during its half-beating. Keeping the former assumption of the single cilium as a rigid rod driven by a constant switching force F^i_{dr}, the average velocity v^i of the cilium during half cycle can be found from

$$\gamma v^i + \gamma v^i \frac{1-\eta_c}{\eta_c} = F^i_{dr} + \gamma v^{nc}_{EX}, \qquad [5]$$

where we introduced $v^{nc}_{EX} = \sum_{j \neq i}^{N} v^{ij}$ as the sum of the average flow velocity v^{ij} produced by the cilium j at the position of the cilium i during its half-beating cycle. This is the average speed of the flow induced by all of the other cilia at the position of the cilium i during its half-beating cycle, if the cilium i were to be removed. As in the previous section, η_c accounts for the internal ciliary dissipation (32, 44). The driving force is again $F^i_{dr} = \gamma v^i_0/\eta_c \approx 2A\gamma(CBF_0)/\eta_c$, and v^i_0 is the cilium average velocity in the absence of any interaction. From Eq. **5**, we estimate that the flow induced by the nearby cilia on the cilium i is

$$v^{nc}_{EX} = (v^i - v^i_0)/\eta_c. \qquad [6]$$

We previously showed that the average velocity of each cilium, v^i, reaches a plateau value v^i_{max} when the number of cilia is sufficiently large. This is valid for hydrodynamically screened cilia within the assumptions made for the IER model. The value of the maximum velocity can be found from $v^i_{max}/v^i_0 = \mathrm{CBF_{max}}/\mathrm{CBF_0} = 1/(1-\eta_c)$ (Eq. **4**). Thus $v^i_{max} = v^i_0/(1-\eta_c)$. Substituting the latter expression into Eq. **6**, we found, in the limit of a large number of cilia,

$$v^{nc}_{EX} = v^i_0 \left[\frac{1}{(1-\eta_c)} - 1\right]/\eta_c = \frac{v^i_0}{(1-\eta_c)}. \qquad [7]$$

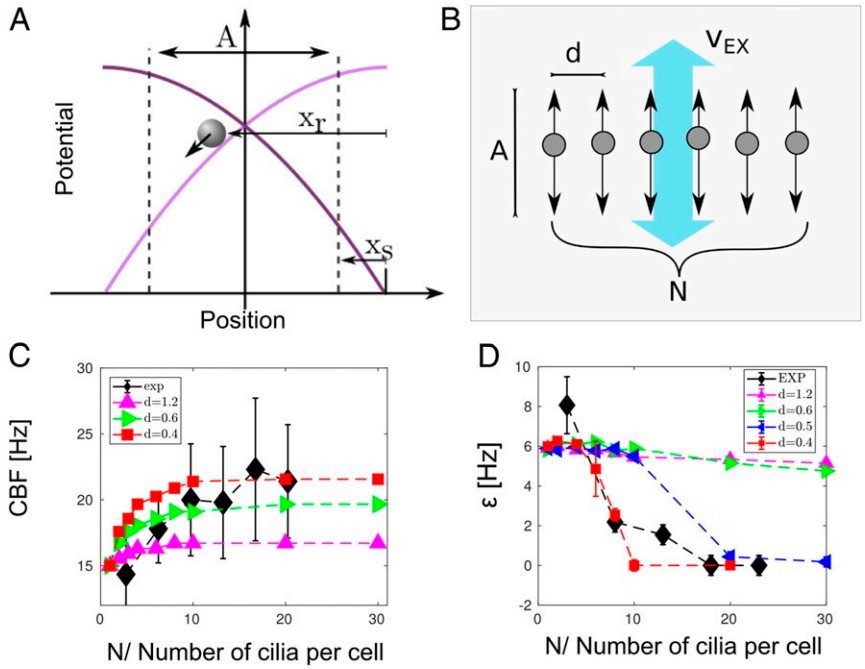

Fig. 5. A coarse-grained model, where each cilium is a hydrodynamically coupled phase oscillator, is studied numerically and recapitulates the main trends seen in the experiment. (*A*) Geometric switch rower oscillator: Two potentials (purple and pink curves) are switched on and off in turn, using feedback control. When one potential is active, it is replaced by the other in the event that the sphere reaches the position indicated by the black dashed line. This active system maintains the sphere in a phase-free oscillation. (*B*) Illustration of the geometry of rower simulation. (*C*) The median frequency of rowers increases with the number of rowers *N*. The growth is more marked as the rowers get closer, $d = [0.4, 0.6, 1.2]$ μm. The trend in simulations of the simple rower model matches with the experimental data (black points are the binned median of the experimentally measured CBF, with SD errors), where the distance between cilia could be smaller ($d_{cilia} \approx 0.2$ μm). (*D*) Chain of rowers under oscillatory external flow. The entrainment strength ϵ decreases as the number of rowers, or their density, increases. For the rowers with distance $d = 0.4$ μm, entrainment was not observed when the number of rowers was $N > 10$. The experimental data, plotted in black, show a similar trend, although the magnitude of the external flow used experimentally was an order of magnitude higher than the one used in simulations, and the distance between cilia is lower (external flows $v_{ex}^{sim} = 30$ μm/s, $v_{EX} = 600$ μm/s).

Therefore, it becomes apparent that, for cilia bundles beating at the maximal frequency $\mathrm{CBF_{max}}$, the flow generated by all other cilia (nearly) sets of the flow generated by a central cilium, $v_{EX}^{nc} = v_{max}^{i}$.

From our measurements, the CBF reaches a plateau for cells with $N > 20$ (see also Fig. 4), and $\mathrm{CBF_{max}} \approx 22$ Hz. Thus, we found $v_{EX}^{nc} = v_{max}^{i} = 2A(\mathrm{CBF_{max}}) \approx 440$ μm/s, with $A = 10$ μm as the beating amplitude. This simple estimate provides a useful measure of the flow generated by the nearby cilia directly on the cilium i during hydrodynamical screening. We previously found that a similar magnitude of oscillatory external flow ($v_{EX} \approx 200$ μm/s) was sufficient to entrain small groups of cilia, and so certainly a single cilium (Fig. 1*D*). We thus expect that the extracted oscillatory cilia-driven flow v_{EX}^{nc} is also sufficient to ensure hydrodynamic entrainment of the cilium i. The same reasoning could be extended for each other cilium j in the cell, suggesting that cilia within a cell could be synchronized through internal hydrodynamic forces. Moreover, the magnitude of the interaction velocity v_{EX}^{nc} is in agreement with the measured flow field near eukaryotic beating cilia with similar lengths (22, 48), and by the net flow generated by ependymal cells in vivo (34), supporting the initial assumption that the measured forces between cilia can have hydrodynamic origin.

Simulations of Hydrodynamically Coupled Oscillators under External Flow. In order to identify whether the dynamics of cilia could stem from hydrodynamic coupling, we compared our data with simulations of simplified cilia coupled hydrodynamically. Building on previous work by our group and others (18), we know that minimal "rower" models in which each cilium is represented by a single sphere driven by a geometrically updated potential can shed light on the effects of synchronization due to cilia arrangement and beating dynamics. This type of model is based on the physical intuition that, in a coarse-grained fashion, the degrees of freedom of the complex cilium shapes and activity can be captured by a rower's driving potential. The main advantage of this approach is that it greatly simplifies the calculation of drag forces, both those acting on the individual object and the force induced by one object on another (49, 50). The sphere moves away from the trap vertex until it reaches the switch point $A + x_s$, where the trap is reflected and the sphere reverses direction. This feedback-controlled motion of the potential is sufficient to induce sustained oscillations, and each sphere undergoes longtime periodic motion with a fixed amplitude but free phase and period. Theoretical and experimental studies showed that pairs and chains of rowers can undergo synchronization (17) and even metachronicity (51, 52) when the separation is sufficiently small. To have a similar scale to the biological system of this work, each cilium is simulated with a rower with radius $a = 0.1$ μm, oscillating with fixed amplitude $A = 7$ μm, tuning the strength of the parabolic trap to ensure an intrinsic frequency $f_0 = 15$ Hz. These values were chosen to be similar to the ones that were found experimentally by tracking a single cilium (*SI Appendix*, Fig. S12). Simulations of chains were performed using a Brownian Dynamics code as in ref. 49, varying the number of N rowers, keeping nearest neighbors separated, on average, by a distance d. We explored the set of $N = [1, 2, 4, 6, 8, 10, 20, 30]$ and $d = [0.4, 0.5, 0.6, 1.2]$ μm (Fig. 5*C*). The rowers are coupled through the hydrodynamic forces via a Blake tensor, with the oscillations occurring at a fixed distance $z_{wall} = 7$ μm above the no-slip boundary (49). For sufficiently small d, the chain of rowers synchronizes through hydrodynamic

forces, and spheres oscillate at a common frequency $f > f_0$, as seen in Fig. 5*C*. As expected, the frequency shift $\delta f = f - f_0$ initially increases with N, before saturating. The increase is more significant for rowers with small separation, due to the increase in their interaction strength. Interestingly, despite the simplicity of the rower model, the order of magnitude of δf in these simulations is the same as observed experimentally, although the latter is consistently lower. This could be explained by the fact that the distance between cilia in the same cell is much smaller ($d \approx 0.1\ \mu$m) than the one that we can simulate (for distances $d \approx a$, near-field effects may play a role that we do not take into account). We then simulated the chain of rowers under an external flow with a magnitude of $v_{EX}^{sim} = 30\ \mu$m/s. The chain was defined as entrained when more than 80% of the rowers were phase-locked with the external flow. Results are shown in Fig. 5*D*. We observe a decrease in the entrainment region as the number of rowers in the chain increases. This effect is more pronounced when the density of the rowers increases. In the most extreme cases, the chain does not entrain with the flow, which is consistent with the experimental data. It is worth noting that, for a given velocity, the smaller chain of rowers is entrained for a much larger range of frequency (for which width is ϵ) than what is observed experimentally; that is, the susceptibility of cilia to an external flow is overestimated by the rower model. One possible reason is because these simulations do not include any intraciliary dissipation (32, 44), and do not attempt to have a realistic geometry for the cilia layout. The simplicity of the model aims to test the proposed origin of coupling, and it captures well the qualitative trends observed in the cilia; we would not expect a quantitative agreement from this model.

Discussion and Conclusions

In the present work, we provide experimental proof of entrainment of mammalian multiciliated cells by hydrodynamic forces. We found the entrainment strength to sharply decrease with the number of cilia. From this main experiment, we combine experimental and theoretical approaches to understand whether hydrodynamic forces between cilia could be responsible for the observed trend. Studying this coupling is useful for the comprehension of the large-scale problem, where thousands of multiciliated cells arranged in packed epithelia display metachronal coordination. Firstly, we measured the hydrodynamic forces required for entrainment of cilia in isolated multiciliated cells. We found that multiciliated cells with few cilia (1–5) are very responsive to external oscillatory flow and can be entrained to a fluid flow around $v_{EX} = 200\ \mu$m/s, similar in magnitude to the one that a cilium can generate during its power and recovery strokes (22) and to the total net flow generated by ciliated cells in the brain (34). These results are in agreement with recent experimental works with *Volvox* somatic cells, where cilia-driven flow is sufficient to produce robust synchrony of isolated flagella pairs (22), while they are in contrast with what was reported in *Chlamydomonas* algae. For this alga, where the elastic coupling between cilia has been shown to be important for the synchronization (25, 26), hydrodynamic forces required for entrainment were measured to be an order of magnitude higher than the physiological ones (24). In agreement with this, pairs of these isolated flagella (in an experiment only coupled through hydrodynamics) do not show stable synchronization (25). By contrast, here we measure a very high susceptibility of motile cilia to external flow, in the same order of the cilia-driven flow reported in literature (22, 48), highlighting the possible different roles of cilia hydrodynamic coupling across microorganisms and mammals. We address the importance of the shape of the cilia waveform, and how that varies across species in connection to cilia function in ref. 53.

We have reported here that the entrainment strength of a cilia bundle decreases with their number. The trend is quantitatively described by a model that accounts for cilia hydrodynamic screening by assuming the group of packed cilia to behave hydrodynamically as an impenetrable rigid rod with an effective radius (that depends on the number of cilia) and accounts for interciliary friction (32). The hydrodynamic screening between cilia was estimated using parameters found in the past literature and measured experimentally. We extracted the chemomechanical beating efficiency of the cilium in agreement with past works with other ciliated organisms (32, 44). Successively, we measured that multiciliated cells with a higher number of cilia were, on average, beating with larger CBF. Again, we could quantitatively describe this trend with cilia effective drag reduction by screening effects and interciliary dissipation. The CBF increase was not affected after depolymerization of the cell actin network, supporting the hypothesis that the measured effect is not driven by the elastic forces transmitted through the cytoskeleton. Moreover, we argue that steric interactions between cilia could not be responsible for the observed trend (*SI Appendix*, section 3). Arguing that CBF increase has only hydrodynamic origin, we estimated the cell-driven flow acting on each cilium in a synchronized multiciliated cell. We found that this flow is quantitatively sufficient to entrain the motility of each cilium within a cell. To further verify the importance of hydrodynamic forces, we carried out simulations of motile cilia, studying the effects of cilia number and external flow, within the minimal model of rowers. In this model, actively driven oscillators interact only through the fluid flow that they create themselves by oscillating. We found that the trends of the simulation results match the experiments on live cilia. Specifically, simulations predict an increase of the CBF with the number and density of cilia that is similar to the one measured. Moreover, they show a threshold with the number of cilia above which the entrainment of a chain of rowers is not possible anymore, as observed experimentally. Overall, the high susceptibility of these cilia to external fluid flow and the magnitude of the hydrodynamic coupling between cilia in a cell suggest that hydrodynamic forces have an important role in the coordination of cilia in the brain. Our results are also important in view of the recent measurement of CSF speed in the bulk and near-wall of the brain. For example, magnetic resonance measurements of the brain (54, 55) demonstrate that CSF in the nervous system moves in an oscillatory fashion due to arterial pressure during heart beat cycle with velocities several orders of magnitude larger than those generated by the cilia, and might have an effect on the coordination of cilia themselves. Moreover, it was recently observed that the cilia-driven flow close to the brain walls follows a complex spatiotemporally regulated network (34). Hydrodynamic screening effects and cilia density in the brain may have played an important role in how CSF established these complex flow networks during development (8).

In our study, we did not focus on the establishment of cilia synchronization, but only on cilia dynamics after synchronization or entrainment is already established. Whether hydrodynamic coupling between cilia is the only coupling that is responsible for cilia synchronization is still unclear and needs to be tackled in future work. Specifically, we cannot firmly rule out that other mechanisms are at play in the synchronization of cilia in the brain—for example, biochemical or mechanical elastic coupling at the bases of the cilia could also contribute to their coordination. It is worth noting that we did not take into account that cilia in multiciliated cells are densely packed, so that steric and other direct repulsive interactions could also play an important role in their synchronization (46, 56). For example, these forces could set the average distance between cilia in the cell. Investigating such effects from an experimental point of view is very challenging. Simulations of hydrodynamic interacting filaments where steric

interaction (in the form of increasingly stiff repulsions) can be tuned and turned on and off seems a more amenable approach to examine this fascinating question. For example, simulations including steric interactions suggest that these forces play a role in the bundle formation of bacteria flagella, together with hydrodynamics (45).

Further experimental investigations are required to validate these results for other mammalian multiciliated cells, especially where cilia propel mucus as in the airways; here cilia beat in a non-Newtonian medium and are also tethered by mucins (57). Hydrodynamic screening due to cilia density may have even larger effects in the airways, where each cell has hundreds of cilia which are constantly subjected to external flows due to breathing.

Methods and Materials

Transwell Chip. PDMS substrates with channel features were bonded to Corning Transwell insert membrane using PDMS prepolymer as glue (58). PDMS prepolymer was mixed with curing agent at a weight ratio of 12:1. The mixture was then cast onto an aluminum mold having positive reliefs of the channels with 1 mm × 1 mm rectangular area and 12 mm long and cured at 60 °C overnight. The mold was produced by Computer Numerical Control (CNC) mill machining. The cured PDMS layer was peeled from the aluminum substrate, and holes of 2-mm diameter were punched through the cured PDMS substrates at the end of the channels. Then PDMS prepolymer with (ratio 10:1) was spin-coated on a clean glass cover slide for 1 min (10 s at 500 rpm, ramped at 500 rpm/s to 3,000 rpm for 60 s) to generate a thin mortar layer (59). This thin PDMS prepolymer serves as "mortar" to strongly bind the PDMS substrate with the membrane. The PDMS substrates with channels were placed onto the glass slides spin-coated with the adhesive PDMS mortar and allowed to stay in contact for 30 s. Then the PDMS substrate were gently placed on Transwell Corning inserts with a polyester membrane of 24-mm diameter and 0.4-μm porosity. The combined pieces were left to cure at room temperature for at least 2 d in six-well plates. Higher curing temperature would result in melting of the glue between the membrane and the insert. Then, two short pieces of tubing of 0.50 inches outer diameter were placed at the inlet and outlet of the channels to facilitate the entrance of fluid using pipettes. Before seeding the cells, the complete Transwell chip was sterilized under ultraviolet for 30 min. PDMS offers many advantages for microfluidic cell culture because of its gas permeability, optical transparency, and flexibility, and has been used in recent decades for long-term culture and cell differentiation of many cell types (60, 61). However, for long-term culture in microfluidics, constant perfusion of media is needed because of the limited nutrients available in the small channel volume (62). For this reason, the PDMS channel was bound to a Corning Transwell insert, where the medium in the basolateral compartment acts as a nutrient reservoir that reaches the cells through the porous membrane. This allows the culture and differentiation of ependymal cells in a channel without the need of media perfusion. We found this extra medium to be a critical requirement for a good differentiation of the NSC in the channel.

Cell Culture. All animal studies were performed in accordance with the guidelines of the European Community and French Ministry of Agriculture and were approved by the Ethics committee Charles Darwin (C2EA-05) and "Direction départementale de la protection des populations de Paris" (Approval number Ce5/2012/107; APAFiS # 9343). The mouse strain Cen2-GFP has already been described (41). Differentiating ependymal cells were isolated from mouse brain and grown in a flask as previously described (33). When cells were 70 to 80% confluent in the T25 Flask, they were seeded at a concentration of 10^7 cells per mL in the Transwell chip in 10% fetal bovine serum, 1% penicillin/streptomycin (P/S) Dulbecco's modified Eagle's medium (DMEM). The day after, the cells were rinsed with phosphate-buffered saline, and medium was switched to 1% P/S DMEM. Medium was not changed during the period of differentiation. After 15 d, cells were fully differentiated. In the culture, a small percentage of multiciliated cells have motile cilia, lacking a common beating direction and frequency. For our analysis, we focused on 58 multiciliated cells from eight different Transwell inserts, with all of the cilia beating in a defined beating direction and showing a single peak spatial frequency distribution. More information on the statistics is provided in *SI Appendix*, Fig. S5.

Solenoidal Pump and Flow Calibration. The inlet of a Transwell insert is connected through tubing to a PDMS chamber fully filled with fresh medium. An alternating flow of medium is created when the top membrane of the elastic chamber is moved up and down by the piston. The oscillations of a soft iron piston are controlled by the magnitude and frequency of alternate current (AC) flowing into a solenoid copper coil around the piston (Fig. 1) and a preloaded spring in a similar fashion to commercially available solenoidal fluid pump. The solenoid was made by wrapping copper wire (0.5 mm) 300 times around an aluminum case for the soft iron piston and the spring. The piston was tightly connected to the top membrane of the PDMS chamber through a screw ending embedded in the PDMS. The PDMS chamber is 5 mm in height with top area 10 mm × 10 mm. The alternate current was created by a function generator connected to a current drive source. The output current was monitored with an oscilloscope through a current proportional voltage output. We tracked 1-μm polystyrene tracer particles to measure the flow and frequency created by the solenoidal pump into the Transwell insert. The calibration was performed in a Transwell chip without cells. Recordings of the oscillating particles were taken at 500 fps and with 40× and 20× objectives at distances of 7, 14, and 21 μm from the wall surface. The average velocities during the half-period were measured by tracking the particle displacements. The minimum applied velocity was chosen to be similar to the flow measured in vivo by tissue ependymal ciliated cells of ∼200 μm/s (34). The maximum applied flow velocity is 10 times the physiologically relevant one. *SI Appendix*, Fig. S4 shows the output flow velocity varying the amplitude and frequency of the AC signal in the solenoid. The generated flow velocity was measured to be higher for low frequency, due to the resonant response of the system.

Image Acquisition and Analysis. Images were taken with a Ti-E inverted microscope (Nikon) equipped with a 60× WI objective 1.20 NA. High-speed

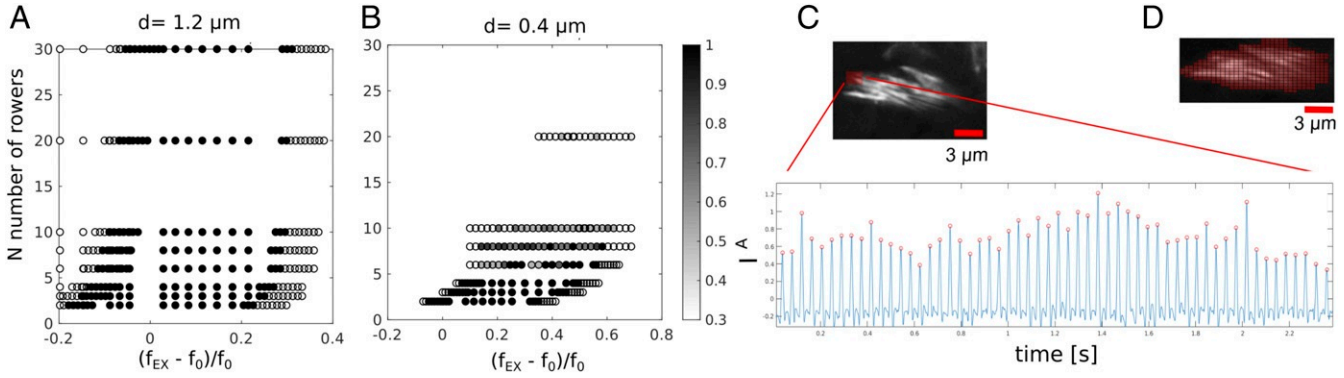

Fig. 6. Simulations and image analysis methods. (*A* and *B*) Simulations: synchronization graphs in frequency domain as a function of the number of rowers, using external flow velocity $v_{EX} = 30$ μm/s for both of the cases. The colormap represents the percentage of rowers synchronized in each simulation; 1 is when 100% of all of the rowers are synchronized with the external force. (*C*) The pixel intensity $I^A(t)$ over time is used to identify the phase of a cilium or cilia within a cell. Each peak is the time when a cilium completes a beat cycle. The interrogation area is indicated in red on the SD map. (*D*) The subimage used for the calculation of the CBF and defined using the SD of the pixel intensities over time.

videos were recorded at 500 fps using a complementary metal–oxide–semiconductor (CMOS) camera (model GS3-U3-23S6M-C; Point Gray Research/FLIR). At each image, a running average of 60 frames was subtracted. To define entrainment events, CBF is measured as the highest peak of the first harmonic of the average periodogram, $P^S(f) = \sum_{px \in S} |\tilde{I_{px}}(f)|^2$, as in refs. 37, 38, and 63, with $\tilde{I_{px}}(f)$ as the FFT over time of the pixel intensity I_{px}, and S as the ensemble of pixels in a subimage thresholded for ciliary motion. The subimage was defined to include all of the pixels for which the SD of the intensity over time is larger than a threshold value (this is found with Matlab function using Otsu's method) (Fig. 6). Entrainment with the external flow is identified when the frequency of the signal highest peak pk^1 coincides with the frequency of the external flow within a certain error σf. For our acquisition rate $\sigma = 0.25$ Hz, the requirement is half of our frequency resolution. This method was implemented for high values of external flow $v_{EX} > 1$ mm/s, when the oscillatory external flow induces a periodic defocusing of the field of view. This effect was detectable in the periodogram and often contributes to the highest peak of the signal, making it more tedious to measure CBF and entrainment events. For this reason, when the first peak of the signal $pk^1 \approx f_{EX}$, we also compared the second higher peak pk^2 to the value of pk_0^1, the signal peak in absence of flow. When $pk^2 > 1/4 pk_0^1$, we identify such entrainment events as false, and identify the second peak as the real contribution from the cell to the signal. This process was found to be valid and stable for every movie that we inspected. For the calculation of the spatial noise ξ_s and cell frequency maps, we measured the frequency on 4×4 pixel boxes over the subimage thresholded for ciliary motion. For each box, we averaged the FFT spectra of the pixel intensity over time, and we identified the frequency corresponding to the higher peak. In some rare cases, we noticed that second harmonics have a higher peak in the spectrum with respect to the first one, leading to erroneous results. These rare events have a relevant effect when calculating the SD of the frequency σ_f, since the SD is very sensible to outliers. Since these events happen rarely and in sparse positions over the cells, we decided to neglect all of the suspected boxes with frequencies that are close to the double of the median frequency and do not have connected boxes with similar frequency (within the range of 2 Hz). We found this step to be critical for a correct calculation of ξ_s. The phase dynamics was calculated by tracking, over time, the pixel intensity of an interrogation area A, chosen to be close to the recovery stroke of the cell, $I^A = -\sum_{px \in A} I_{px}$. This area is small, such that only one or, at most, two cilia can be detected per time. When a cilium passes through this area, the pixel intensity I^A spikes (Fig. 6). The time of the spike is an indication that the cilium completed a cycle, and the phase of the cilium ϕ_{cilium} increases by 2π. The number of cilia per cell was counted by inspection of movies at 500 fps, after median filtering (window of 3×3 pixels) and contrast correction. All of the analyses were performed in Matlab.

Simulations. The simulation scheme builds on previous work (36, 49, 50) but implements external flow on an array of active phase-free oscillators. Rowers are driven by repulsive harmonic traps, with the potential $U(x_r) = k x_r^2$. The traps are updated when $x_r > A + x_s$, with the switch condition $x_s = 1$ μm and the amplitude $A = 7$ μm. The spheres themselves have a radius $a = 0.1$ μm, and their position is updated via an equation,

$$\frac{d\mathbf{x}_i}{dt} = \sum_{j=1}^{N} \mathbf{H}_{ij}\mathbf{F}_j + v_{EX}^{sim}. \quad [8]$$

The rowers are coupled through the Blake tensor **H**. The tensor is implemented in a plane at a constant height above the no-slip boundary, $h = 7$ μm (49). The drag is $\gamma = 6\pi\eta a$, where $\eta = 0.0022$ Pa·s. Note that we have chosen to report here dimensional units to make the comparison with experiments more straightforward; the parameters in the simulation are chosen to give CBF and forces of similar order of magnitude to the biological system. The external flow v_{EX}^{sim} is implemented as a square wave, it has an amplitude v_e, and it changes direction every N_f frames. The switching results in a period $N_f \delta t$, where δt is the simulation time step.

The simulations were run for 10 s (150 cycles), with time step $\delta t = 3 \cdot 10^{-5}$ s ($9 \cdot 10^{-4}$ cycles). Each case was repeated 10 times, with the initial positions of each rower within the trap drawn from a uniform distribution $U \approx [-A/2, A/2]$. The entrainment strength ϵ is calculated for each seed, and the average is reported here.

To determine the entrainment strength for each set of simulations, first, each rower is classified as entrained or not by considering its phase relative to that of the external flow. A rower is entrained if, after the initial transient period (3 s), fewer than five phase slips occur. This accounts for edge effects that appear in longer chains. The chain is considered phase-locked if 80% of the rowers are entrained, with rowers near the edges excluded from the sample. Finally, an ϵ is measured by calculating the range of frequencies in which the chain is phase-locked. For the longer chains in high density, this approach was not possible, for the range of frequencies where chains were considered phase-locked also included simulations with too few rowers entrained to be classified as phase-locked. The greater variability in the number of entrained rowers likely stems from coexistence of two stable states, entrained and not entrained, during the transition from a chain that can be phase-locked to one too strongly coupled to do so. Instead, in these cases, the sum of phase-locked cases is multiplied by the resolution of the frequency sampling $0.017 f_0$ to give an estimate of ϵ. The measurement for ϵ across each case is repeated for the 10 simulations sets, and the average is plotted in Fig. 5. Further details regarding the steps to measure ϵ are described in *SI Appendix*, section 2.

Data Availability. A frequency scan dataset for a cell is available as a Zenodo repository, https://doi.org/10.5281/zenodo.3604352, and the complete set of movie files supporting this paper is available on request to the authors.

ACKNOWLEDGMENTS. We thank B. Friedrich, E. Lauga, D. Das, and C. Maggi for stimulating discussions. N.P. and P.C. were supported by the European Union Horizon 2020 research and innovation program under Marie Sklodowska-Curie Grant 641639 ITN BioPol; P.C. and J.K. were also supported by European Research Council (ERC) CoG HydroSync; and E.H. was supported by Cambridge Trusts. M.F., N.D., and N.S. were supported by INSERM, CNRS, École Normale Supérieure, and ERC CoG Grant 647466.

1. J. R. Blake, M. A. Sleigh, Mechanics of ciliary locomotion. *Biol. Rev.* **49**, 85–125 (1974).
2. E. W. Knight-Jones, Relations between metachronism and the direction of ciliary beat in metazoa. *J. Cell Sci.* **3**, 503–521 (1954).
3. J. V. Fahy, B. F. Dickey, Airway mucus function and dysfunction. *N. Engl. J. Med.* **363**, 2233–2247 (2010).
4. G. R. Ramirez-San Juan *et al.*, Multi-scale spatial heterogeneity enhances particle clearance in airway ciliary arrays. bioRxiv:665125 (9 June 2019).
5. K. Sawamoto *et al.*, New neurons follow the flow of cerebrospinal fluid in the adult brain. *Science* **311**, 629–632 (2006).
6. M. Fliegauf, T. Benzing, H. Omran, When cilia go bad: Cilia defects and ciliopathies. *Nat. Rev.* **8**, 880–893 (2007).
7. B. Mitchell, R. Jacobs, J. Li, S. Chien, C. Kintner, A positive feedback mechanism governs the polarity and motion of motile cilia. *Nature* **447**, 97–101 (2007).
8. B. Guirao *et al.*, Coupling between hydrodynamic forces and planar cell polarity orients mammalian motile cilia. *Nat. Cell Biol.* **12**, 341–350 (2010).
9. M. J. Sanderson, M. A. Sleigh, Ciliary activity of cultured rabbit tracheal epithelium: Beat pattern and metachrony. *J. Cell Sci.* **47**, 331–347 (1981).
10. S. Gueron, K. Levit-Gurevich, Energetic considerations of ciliary beating and the advantage of metachronal coordination. *Proc. Natl. Acad. Sci. U.S.A.* **96**, 12240–12245 (1999).
11. H. M. Oliveira, L. V. Melo, Huygens synchronization of two clocks. *Sci. Rep.* **5**, 11548 (2015).
12. G. I. Taylor. Analysis of the swimming of microscopic organisms. *Proc. Roy. Soc. Lond.* **209**, 447–461 (1951).
13. A. Vilfan, F. Julicher, Hydrodynamic flow patterns and synchronization of beating cilia. *Phys. Rev. Lett.* **96**, 058102 (2006).
14. J. Elgeti, G. Gompper, Emergence of metachronal waves in cilia array. *Proc. Natl. Acad. Sci. U.S.A.* **110**, 4470–4475 (2013).
15. B. Guirao, J. F. Joanny, Spontaneous creation of microscopic flow and metachronal waves in an array of cilia. *Biophys. J.* **92**, 1900–1917 (2007).
16. T. Niedermayer, B. Eckhardt, P. Lenz, Synchronization, phase locking, and metachronal wave formation in ciliary chains. *Chaos* **18**, 037128 (2008).
17. J. Kotar, M. Leoni, B. Bassetti, M. C. Lagomarsino, P. Cicuta, Hydrodynamic synchronization of colloidal oscillators. *Proc. Natl. Acad. Sci. U.S.A.* **107**, 7669–7673 (2010).
18. N. Bruot, P. Cicuta, Realizing the physics of motile cilia synchronization with driven colloids. *Ann. Rev. Condens. Matter Phys.* **7**, 1–15 (2016).
19. S. L. Tamm, T. M. Sonneborn, R. V. Dippell, The role of cortical orientation in the control of direction of ciliary beat in paramecium. *J. Cell Biol.* **64**, 98–112 (1975).
20. H. Machemer, Ciliary activity and the origin of metachrony in paramecium: Effects of increased viscosity. *J. Exp. Biol.* **57**, 239–259 (1972).
21. M. Polin, I. Tuval, K. Drescher, J. P. Gollub, R. E. Goldstein, Chlamydomonas swims with two "gears" in a eukaryotic version of run-and-tumble locomotion. *Science* **325**, 487–490 (2009).
22. D. R. Brumley, K. Y. Wan, M. Polin, R. E. Goldstein, Flagellar synchronization through direct hydrodynamic interactions. *eLife* **3**, e02750 (2014).
23. D. R. Brumley, M. Polin, T. J. Pedley, R. E. Goldstein, Hydrodynamic synchronization and metachronal waves on the surface of the colonial alga volvox carteri. *Phys. Rev. Lett.* **109**, 268102 (2012).

24. G. Quaranta, M.-E. Aubin-Tam, D. Tam, Hydrodynamics versus intracellular coupling in the synchronization of eukaryotic flagella. *Phys. Rev. Lett.* **115**, 238101 (2015).
25. K. Y. Wan, R. E. Goldstein, Coordinated beating of algal flagella is mediated by basal coupling. *Proc. Natl. Acad. Sci. U.S.A.* **113**, 2784–2793 (2016).
26. K. C. Leptos *et al.*, Antiphase synchronization in a flagellar-dominance mutant of chlamydomonas. *Phys. Rev. Lett.* **111**, 158101 (2013).
27. Y. Liu, R. Claydon, M. Polin, D. R. Brumley, Transitions in synchronization states of model cilia through basal-connection coupling. *J. R. Soc. Interface* **15**, 20180450 (2018).
28. G. S. Klindt, C. Ruloff, C. Wagner, B. M. Friedrich, In-phase and anti-phase flagellar synchronization by waveform compliance and basal coupling. *New J. Phys.* **19**, 113052 (2017).
29. A. Mahuzier *et al.*, Ependymal cilia beating induces an actin network to protect centrioles against shear stress. *Nat. Commun.* **117**, 094101 (2017).
30. E. K. Vladar, R. D. Bayly, A. M. Sangoram, M. P. Scott, J. D. Axelrod, Microtubules enable the planar cell polarity of airway cilia. *Curr. Biol.* **22**, 2203–2212 (2012).
31. M. E. Werner *et al.*, Actin and microtubules drive differential aspects of planar cell polarity in multiciliated cells. *J. Cell Biol.* **195**, 19–26 (2011).
32. G. S. Klindt, C. Ruloff, C. Wagner, B. M. Friedrich, Load response of the flagellar beat. *Phys. Rev. Lett.* **117**, 258101 (2016).
33. N. Delgehyr *et al.*, Ependymal cell differentiation, from monociliated to multiciliated cells. *Methods Cell Biol.* **127**, 19–35 (2015).
34. R. Faubel, C. Westendorf, E. Bodenschatz, G. Eichele, Cilia-based flow network in the brain ventricles. *Science* **353**, 176–178 (2016).
35. A. Pikovsky, M. Rosenblum, J. Kurths, *Synchronization: A Universal Concept in Nonlinear Sciences* (Cambridge University Press, 2003), vol. 12.
36. N. Bruot, L. Damet, J. Kotar, P. Cicuta, M. C. Lagomarsino, Noise and synchronization of a single active colloid. *Phys. Rev. Lett.* **107**, 094101 (2011).
37. S. Dimova *et al.*, High-speed digital imaging method for ciliary beat frequency measurement. *J. Pharm. Pharmacol.* **57**, 521–526 (2005).
38. J. H. Sisson, J. A. Stoner, B. A. Ammons, T. A. Wyatt, All-digital image capture and whole-field analysis of ciliary beat frequency. *J. Microscopy* **211**, 103–111 (2003).
39. E. Lauga, T. R. Powers, The hydrodynamics of swimming microorganisms. *Rep. Prog. Phys.* **72**, 096601 (2009).
40. C. Allain, M. Cloitre, The effects of gravity on the aggregation and the gelation of colloids. *Adv. Colloid Interface Sci.* **46**, 129–138 (1993).
41. H. Higginbotham, S. Bielas, T. Tanaka, J. G. Gleeson, Transgenic mouse line with green-fluorescent protein-labeled centrin 2 allows visualization of the centrosome in living cells. *Transgenic Res.* **13**, 155–164 (2004).
42. A. J. Hunt, F. Gittes, J. Howard, The force exerted by a single kinesin molecule against a viscous load. *Biophys. J.* **67**, 766–781 (1994).
43. B. M. Friedrich, Load response of shape-changing microswimmers scales with their swimming efficiency. *Phys. Rev. E* **97**, 042416 (2018).
44. C. J. Brokaw, Adenosine triphosphate usage by flagella. *Science* **156**, 76–78 (1967).
45. S. Y. Reigh, R. G. Winkler, G. Gompper, Synchronization and bundling of anchored bacterial flagella. *Soft Matter* **8**, 4363–4372 (2012).
46. Y. Yang, V. Marceau, G. Gompper, Swarm behavior of self-propelled rods and swimming flagella. *Phys. Rev. E* **82**, 031904 (2010).
47. Y. Sassa, S. Shibata, Y. Iwashita, Y. Kimura, Hydrodynamically induced rhythmic motion of optically driven colloidal particles on a ring. *Phys. Rev. E* **85**, 061402 (2012).
48. K. Drescher, R. E. Goldstein, N. Michel, M. Polin, I. Tuval, Direct measurement of the flow field around swimming microorganisms. *Phys. Rev. Lett.* **105**, 168101 (2010).
49. E. Hamilton, N. Bruot, P. Cicuta, The chimera state in colloidal phase oscillators with hydrodynamic interaction. *Chaos* **27**, 123108 (2017).
50. E. Hamilton, P. Cicuta, Interpreting the synchronisation of driven colloidal oscillators via the mean pair interaction. *New J. Phys.* **20**, 093028 (2018).
51. M. C. Lagomarsino, P. Jona, B. Bassetti, Metachronal waves for deterministic switching two-state oscillators with hydrodynamic interaction. *Phys. Rev. E* **68**, 021908 (2003).
52. C. Wollin, H. Stark, Metachronal waves in a chain of rowers with hydrodynamic interactions. *Eur. Phys. J. E* **34**, 42 (2011).
53. E. Hamilton, N. Pellicciotta, L. Feriani, P. Cicuta, Motile cilia hydrodynamics: Entrainment versus synchronisation when coupling through flow. *Philos. Trans. R. Soc. B* **375**, 20190152 (2020).
54. A. Stadlbauer, E. Salomonowitz, W. Van Der Riet, M. Buchfelder, O. Ganslandt, Insight into the patterns of cerebrospinal fluid flow in the human ventricular system using MR velocity mapping. *Neuroimage* **51**, 42–52 (2010).
55. N. Spassky, A. Meunier, The development and functions of multiciliated epithelia. *Nat. Rev. Mol. Cell Biol.* **18**, 423–436 (2017).
56. S. Y. Reigh, R. G. Winkler, G. Gompper, Synchronization, slippage, and unbundling of driven helical flagella. *PLoS One* **8**, e70868 (2013).
57. B. Button *et al.*, A periciliary brush promotes the lung health by separating the mucus layer from airway epithelia. *Science* **337**, 937–941 (2012).
58. D. Trieu, T. K. Waddell, A. P. McGuigan, A microfluidic device to apply shear stresses to polarizing ciliated airway epithelium using air flow. *Biomicrofluidics* **8**, 064104 (2014).
59. B. Chueh *et al.*, Leakage-free bonding of pourous membranes into layered microfluidic array system. *Anal. Chem.* **79**, 3504–3508 (2007).
60. K. H. Benam *et al.*, Small airway-on-a-chip enables analysis of human lung inflammation and drug responses in vitro. *Nat. Methods* **13**, 151–157 (2015).
61. A. Tourovskaia, X. Figueroa-Masot, A. Folch, Differentiation-on-a-chip: A microfluidic platform for long-term cell culture studies. *Lab Chip* **5**, 14–19 (2005).
62. L. Kim, Y.-C. Toh, J. Voldman, H. Yu, A practical guide to microfluidic perfusion culture of adherent mammalian cells. *Lab Chip* **7**, 681–694 (2007).
63. M. Ryser, A. Burn, T. H. Wessel, M. Frenz, J. Rička, Functional imaging of mucociliary phenomena. *Eur. Biophys. J.* **37**, 35–54 (2007).